When there is a discrepancy between the information in this technical report and information in JDox, assume JDox is correct.

STScI | SPACE TELESCOPE SCIENCE INSTITUTE

JWST TECHNICAL REPORT

Title: NIRISS Cycle 2 Calibration Results: AMI Pixel Placement (CAL-NIS-212, PID 4478)	Doc #: JWST-STScI-009186, SM-12 Date: 30 September 2025 Rev: -
Authors: Rachel Cooper, Deepashri Thatte, Anand Sivaramakrishnan Phone: 410-338-6847	Release Date: 17 November 2025

1 Abstract

The goal of JWST Cycle 2 calibration program 4478 (CAL-NIS-212) is to verify whether subpixel offsets applied to the aperture definitions for each filter in May 2023 improved the accuracy of AMI PSF placement. The program contains observations of two single stars in the AMI mode with the three medium-band filters to test that the star can be positioned consistently at the center of a pixel. Having a consistent position for the observations in different filters is helpful in the analysis of the amplitudes and phases of the interference pattern observed through the Non-Redundant Mask (NRM) and should improve the AMI sensitivity. The ability to accurately place the PSF within the pixel is also important for users wishing to place the target on or near a pixel boundary to mitigate effects from charge migration or avoid saturation in the peak pixel with bright targets. This report presents an analysis of the data obtained for PID 4478 in addition to other PSF reference star observations obtained since the filter-dependent aperture positions became active onboard. We describe our implementation of a variation on the Anderson-King method for accurate astrometric measurements and find that the applied offsets do significantly improve the PSF placement accuracy across the three filters tested: average measured offset from the pixel center is now less than five milliarcseconds in F380M, F430M, and F480M.

2 Introduction

Commissioning measurements of the line-of-sight pointing stability of the JWST science instruments under fine guiding control revealed exquisite precision of ~1 mas, symmetric in each axis, better even than the pre-flight predictions of 6-7 mas (Rigby et al. 2022). While such precise and accurate guiding is a *necessity* for a variety of science goals, it benefits all science programs. NIRISS Aperture Masking Interferometry (AMI) observations are not subject to such stringent pointing requirements as, e.g., MIRI coronography, but nevertheless repeatable and precise pointing is critical for optimal AMI calibration. Placing the reference star as close as possible to the subpixel position of the science target minimizes the possibility of systematic

differences altering the interferometric observables. Placing observations of a target in multiple filters at the same subpixel location improves calibration for the same reasons and allows for better multiwavelength comparison. Precise pointing may also allow AMI to reach higher contrasts than anticipated, as placing the target near a pixel boundary or corner splits the peak flux over multiple pixels and may allow for more reads up the ramp below the saturation limit or charge migration threshold, rather than saturating earlier in a single pixel. Additionally, since charge migration is dependent on the signal level and the contrast between adjacent pixels, having the capability of placing the source closer to or further from a pixel boundary may allow for better control of the charge migration.

One of the secondary analysis goals of the AMI science readiness commissioning program, PID 1093, was to test that each primary-dithered exposure was not more than ¼ pixel from the commanded location at the pixel center. Using the nominal isotropic NIRISS pixel scale of 65.6 mas/px, ¼ pixel corresponds to a positional error of 16.4 mas, about a factor of three larger than the demonstrated pointing performance of the observatory. The commissioning measurements exceeded this threshold and displayed an apparent dependence on filter, suggesting a calibration issue due to boresight offsets between the filters (Sivaramakrishnan et al. 2023). We calculated mean offsets for each of the three medium-band AMI filters and used these to define new filter-dependent apertures, which were included in the Science Instrument Aperture File (SIAF) with PRDOPSSOC-061 (May 2023). The filter-dependent apertures were implemented in conjunction with an update to the Astronomer's Proposal Tool (APT), which selects the SIAF aperture associated with the filter for each observation, so there is no loss of efficiency – previously, only one aperture could be used for each observation. This change was introduced in APT 2023.5.

By defining each aperture with a reference position at the opposite of the mean measured offset for that filter, we hoped to see an improvement in the measured centroid with respect to the pixel center that would bring all three filters to a common position, modulo the inherent positional error introduced by WFE, jitter, and other upstream optical effects.

3 Observations

Calibration program 4478 consists of observations of two single stars, HD-37093 and HD-36805, with the three medium-band AMI filters (F380M, F430M, F480M). The exposures are summarized in Table 1. These are the same two stars used as reference stars for AMI commissioning program 1093. Offsets to position the target in the center of the pixel were included as a special requirement because the updates to the SIAF were not yet active when the program was executed on September 2, 2023. The standard AMI target acquisition procedure was followed, wherein the target is first placed in the 64 x 64 pixel SUBTAAMI subarray which is located adjacent to the AMI SUB80 subarray. Three dithered NIS_TACQ exposures are followed by a TA_CONFIRM confirmation image. All AMI target acquisitions use the F480M filter and either the NRM or the CLEARP pupil element depending on the magnitude of the source; both targets for this program used the NRM. Following successful acquisition, the target is moved via small angle maneuver (SAM) to the requested science position. Slews between 60 mas and 25" are performed by halting closed-loop fine guiding, slewing to the new position, and then resuming "track" followed by "fine guide" FGS operation modes. The uncertainty introduced by all types of small slews was found to be ~2-4 mas on each axis (Rigby et al. 2022).

Table 1. Summary of the exposures taken for PID 4478 (excluding Target Acquisition exposures)

Filename	Target	Filter	Ints	Groups	Exposure Start
jw04478001001_03102_00001_nis	HD-37093	F480M	64	10	2023-09-02 09:50:02.890
jw04478002001_03102_00001_nis	HD-37093	F430M	82	7	2023-09-02 10:13:28.366
jw04478003001_03102_00001_nis	HD-37093	F380M	95	4	2023-09-02 10:36:01.476
jw04478004001_03102_00001_nis	HD-36805	F480M	69	7	2023-09-02 11:12:39.376
jw04478005001_03102_00001_nis	HD-36805	F430M	86	5	2023-09-02 11:35:02.315
jw04478006001_03102_00001_nis	HD-36805	F380M	131	2	2023-09-02 11:56:41.769

Additional PSF reference observations taken during GO and other calibration programs following the SIAF update were also analyzed. They are listed in appendix Table 6. Due to the paucity of F277W exposures, we do not report a mean offset for this filter.

4 Method

Prior to launch, with only simulations and ground testing as predictors of data quality, we decided to use a modified version of the algorithm for accurate astrometry described in Anderson & King (2000, hereafter the Anderson-King or AK method). This method uses the concept of the "effective PSF" (ePSF), or the empirical representation of how a point source's light is distributed in each pixel of a telescope image. The ePSF is dependent on the offset of the source's center relative to the pixel center and requires no prior knowledge of pixel-to-pixel variations. Conversely, the instrumental PSF (iPSF) is the image of a point source formed at the focal plane of the telescope and therefore can never be directly observed – to disentangle the true analytical iPSF from the detector effects requires knowledge of the sensitivity profile of each pixel. By fitting the ePSF to our data instead, we do not need to know the sensitivity profile and iPSF separately; we merely measure the value of the ePSF at discrete detector positions, which is in fact the integral of the iPSF over the sensitivity profile of a given pixel. With sufficiently accurate simulated PSFs, we should be able to use this method to recover centroids in NIRISS AMI exposures despite the coarse pixel sampling of the shorter-wavelength AMI filters.

As input to the AK code we use the standard calints.fits products of the `jwst calwebb_image2` pipeline, which have been corrected for most detector-level effects. There may still be NaNs present in the core of the target image at this stage of the data reduction; the effect of bad pixels on the accuracy of centroiding has not been closely examined with in-flight data, but we expect that saturated images in which multiple core pixels have been replaced with NaNs would not contain enough information to yield an accurate centroid. This was demonstrated with one of the additional exposures we used to measure the post-SIAF-update offsets; see Section 5.1 for more information.

A brief description of our code implementation follows. The code can be found on the NIRISS GitLab repository for internal users.

1. Use header information from the data to construct a matching oversampled model

PSF using STPSF (formerly WebbPSF; Perrin et al. 2012, 2014). The observation date is used to retrieve the closest-in-time optical path difference (OPD) measurements from routine wavefront sensing operations. The PSF also matches the filter and commanded detector position of the data. If a matching PSF using the identified OPD at the requested oversampling and detector position already exists in the output directory, it will be used.

2. Make cutouts of data and model around the commanded position: for a data cutout of N x N detector pixels, the model cutout should be N+2 x N+2 detector pixels to allow complete overlap of the model and data cutouts at each position when displaced relative to each other.
3. Iterate over each possible location within the central pixel (determined by the oversampling factor), cutting out a corresponding sub-cutout from the model at each position and rebinning it to detector scale. Save these numpy arrays for re-use; if an appropriate lookup table for a given observation already exists, it will be used.
4. Calculate the minimum absolute difference (MAD) between the data cutout and each of the displaced model cutouts. The difference array with the smallest sum gives the best-fit location of the center of the PSF. The position of the target relative to the commanded position or to the pixel center (the implicit commanded position for primary dithers) can then be deduced. We use the MAD rather than any comparable metric because of its relative insensitivity to outlier noise.

The full Anderson-King method uses an iterative approach and interpolates between detector positions to make precise astrometric measurements of multiple sources in an image. We apply a simplified version, where the precision of our recovered centroids is limited by the inverse of the model PSF oversampling factor, e.g., with an oversampling factor of 11, there are only 121 possible positions within the central pixel, and without interpolating between positions, we will see a "quantization" of the recovered offsets. As the code runtime is highly dependent on the oversampling factor, the need for precision must be weighed against the need for quick results. Future improvements in the code may incorporate a weighting scheme to obtain intermediate values without significant performance cost.

The first version of this code, which was used to calculate the commissioning offsets on which the SIAF updates are based, made several simplifications that limited its functionality. It assumed that the commanded pixel position is always at the pixel center. This is nominally true only for the primary dither positions, so the results are misleading for subpixel dithered or offset data. It also did not specify the NIRISS detector position at which to place the STPSF model, so by default, it was placed at the center of the detector (1024,1024), with the result that these simulations did not correctly capture the distortion at the real location in the SUB80 subarray. It also used a flat wavefront OPD, but centroid movements scale linearly with the mean wavefront tilt over the NRM subapertures, so it is important to attempt to match the OPD at the time of observation if possible (Holfeltz et al. 2015). The changes in the updated AK code mean that it is less efficient, as multiple highly oversampled PSFs may need to be generated in each filter for a dataset, but it is more accurate and can be used to measure AMI centroids at any pixel position.

4.1 Commissioning Measurements

The offsets given in Table 2 were originally measured from commissioning data and used to

define the new SIAF apertures. The offsets are averaged from all the primary-dithered AMI commissioning exposures in PID 1093. The exposures in observations 12, 15, and 18 were taken at primary dither position 1, while 13, 16, and 19 were taken at dither position 2. They were split into separate observations because the AMI team chose to re-define detector position 2 following the unsuccessful first execution of the commissioning program due to a TA algorithm issue. In the re-executed program, the offset to the new "position 2" was applied by specifying offsets in arcseconds in the Special Requirements section of the APT file.

Table 2. Mean offsets in X and Y (detector frame) measured from primary-dithered commissioning exposures

Filter	Mean X [px]	Mean Y [px]	Mean X [mas]	Mean Y [mas]
F380M	0.102 ± 0.029	-0.297 ± 0.020	7.997 ± 2.45	-25.278 ± 3.18
F430M	0.147 ± 0.030	-0.130 ± 0.028	-11.220 ± 2.50	-9.995 ± 3.02
F480M	0.063 ± 0.033	-0.216 ± 0.028	4.091 ± 2.73	-16.383 ± 2.70

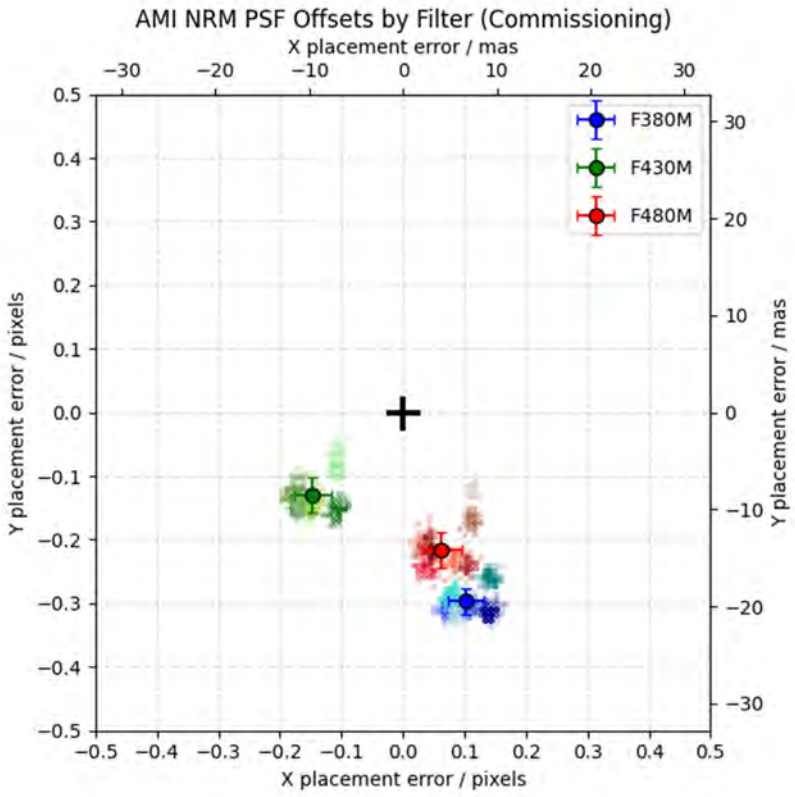

Figure 1. Offsets from the pixel center for twelve primary-dithered exposures collected during instrument commissioning (PID 1093). The individual points composing each small cloud of a given color indicate offsets for each integration of the exposure. The mean offsets for the three AMI filters are shown. The area of the plot corresponds to a single detector pixel; the center of the pixel is indicated by the black cross.

The offsets from the commissioning data, measured with the original AK code implementation, are shown in Figure 1. A version of this figure was originally published in Sivaramakrishnan et al. (2023).

The offsets are applied in the SIAF by adjusting the aperture reference position (in detector X-Y coordinates) to negate the measured per-filter offsets. Prior to this update, the reference pixel position for the first AMI primary dither position (SIAF aperture NIS_AMI1) was (46.0, 41.0). The updated reference positions for the per-filter apertures are in Table 3. Note that SIAF definitions are 1-indexed but Python arrays are 0-indexed, so using these definitions directly as array indices can result in off-by-one errors. This is accounted for in our implementation of the Anderson-King method.

Table 3. SIAF reference positions for apertures defined for each AMI filter, as of PRDOPSSOC-69.

Aperture Name	XSciRef	YSciRef
NIS_AMI1_F277W_NRM	46.436	40.953
NIS_AMI1_F380M_NRM	45.895	41.29
NIS_AMI1_F430M_NRM	46.143	41.121
NIS_AMI1_F480M_NRM	45.995	41.214

4.2 Anderson-King vs. 2D Gaussian Centroiding

Earlier work compared the accuracy and precision of different `photutils` centroiding functions when applied to simulated data (Goudfrooij 2022, JWST-STScI-008116). This work used realistic MIRAGE simulations of the astrometrically well-calibrated "JWST Calibration Field" in the Large Magellanic Cloud. They compared the centroids returned by each method to their known locations from the astrometric catalogue and found that among `photutils.centroids.centroid_com`, `photutils.centroids.centroid_2dg`, `photutils.centroids.centroid_quadratic`, `photutils.detection.DAOStarFinder`, and `photutils.detection.IRAFStarFinder`, the `centroid_2dg` function was found to return the most accurate centroids overall. It has the additional strength of being relatively insensitive to proximity to pixel boundaries, which is a weakness of some of the other methods tested. However, these tests were only performed with regular imaging data, i.e. with the CLEAR or CLEARP pupil element, which produces a more Gaussian PSF than the NRM.

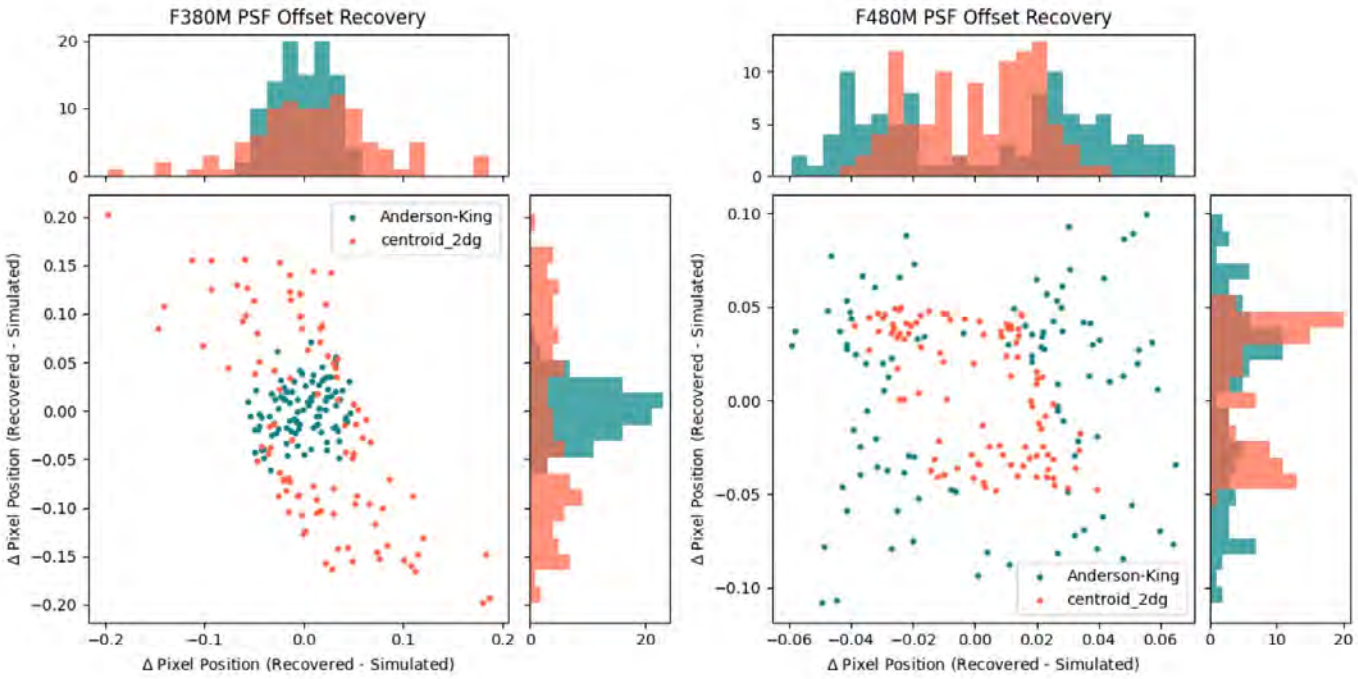

Figure 2. Comparison of performance of Anderson-King and `photutils centroid_2dg` performance on PSFs with known offsets simulated with STPSF in F380M and F480M. The scattered points indicate the difference between the recovered and simulated positions; the associated histograms show the distribution of those differences in X and Y for each method.

To test the accuracy of the centroids recovered using the AK code and compare them to those from the out-of-the-box `centroid_2dg` function, we generated a set of 100 simulated AMI PSFs with random offsets between [-1,1] detector pixels (so they can be as much as √2 pixels radially from the center of the central pixel). We added a reasonable approximation of Poisson noise and read noise to PSFs simulated with STPSF for the F380M and F480M filters. We applied both the AK code and the `centroid_2dg` to each, using a five-pixel box for both and an oversampling of 121 for the AK code. As anticipated, the AK code returns more accurate centroids for the more coarsely sampled F380M PSFs, while `centroid_2dg` was slightly more accurate for the longer wavelength F480M simulations (Figures 2 and A-1).

For F380M, the centroids recovered using the AK method do not show any correlation with simulated distance from the center of the central pixel, while the `centroid_2dg` results shows a strong dependence – the best-fit linear slope is 0.115, compared to the nearly-flat slope of -0.004 for the AK data, shown in Figure 3. In F480M, both methods showed only a small positive correlation between distance from the pixel center and accuracy of the recovered offset. These tests confirm that while this implementation of the AK method is far more computationally expensive than the readily available centroiding algorithms, it performs better for shorter-wavelength AMI data, especially in cases where the source is far from its expected position.

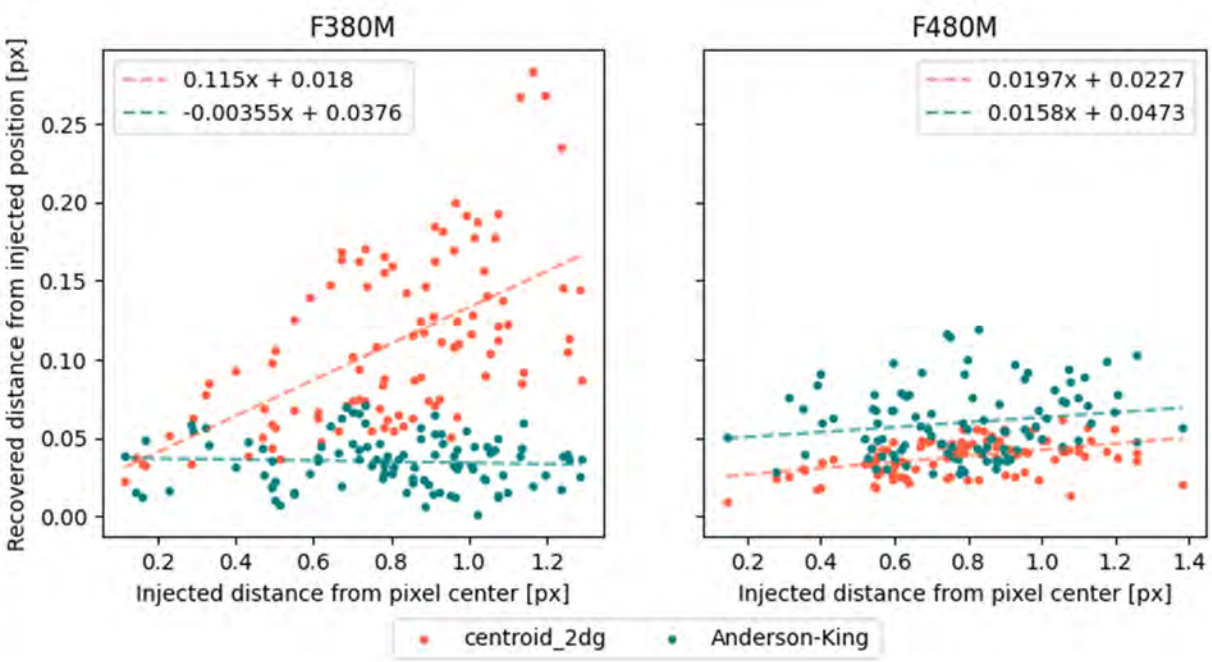

Figure 3. Distance from recovered pixel position as a function of simulated distance from the center of the pixel for the two centroiding methods, in F380M and F480M. There is a positive correlation between the error of the centroid_2dg results and the distance from the pixel center, while the AK method performs consistently well at all tested distances in F380M. In F480M, both methods perform similarly well at all distances.

5 Results

As calibration program 4478 consists of only two exposures in each of the three medium-band AMI filters, we collected all AMI PSF reference star exposures that were available at the time of analysis to expand our sample. We applied the AK code with a five-pixel cutout size and an oversampling factor of 121 to obtain the offset from commanded position for each integration of each exposure to within $1/121^2$ of a pixel (~0.005 mas). While the AK code returns offsets rather than positions, it is trivial to use the commanded position and measured offset to retrieve the subpixel position, and from there calculate the distance to the pixel center (the implicit commanded position when using the per-filter SIAF apertures).

5.1 Revised offsets

Table 4 gives the mean X and Y offsets from the pixel center (in pixels and milliarcseconds) for each filter before the SIAF updates. The same primary-dithered commissioning observations as were used to calculate the offsets for the SIAF were analyzed to obtain these values, although they vary slightly from those reported in Table 2, as the updated version of the AK code was used for consistency with the new measured mean offsets. The source of the difference is most likely from the use of the OPD and accurate distortion in the updated measurements.

Table 4. Mean offsets from the pixel center from commissioning data, re-measured with the updated AK code.

Filter	Mean X [px]	Mean Y [px]	Mean X [mas]	Mean Y [mas]
F380M	0.1219 ± 0.037	-0.3853 ± 0.049	7.9974 ± 2.451	-25.2783 ± 3.184
F430M	-0.1710 ± 0.038	-0.1524 ± 0.046	-11.2199 ± 2.495	-9.9953 ± 3.028
F480M	0.0624 ± 0.042	-0.2497 ± 0.041	4.0910 ± 2.730	-16.3825 ± 2.703

Mean measured X and Y offsets calculated from all primary-dithered PSF reference star observations following the SIAF update are given in Table 5. The use of the per-filter apertures significantly improved the accuracy of target placement for AMI, reducing the mean offset on both axes to less than 5 mas in all three filters. The improvement introduced here is satisfactory, as the pointing uncertainty of the near-infrared science instruments following target acquisition is ~5.5 mas (Sohn et al., in prep). As expected, the mean difference from the actual commanded position (rather than the pixel center) remains the same, as no changes to the TA or fine-guiding procedures were made. The mean jitter (1σ, radial) of the individual exposures used in this analysis is 0.074 mas.

Table 5. Mean offsets from the pixel center for all primary-dithered AMI reference star exposures using the per-filter aperture definitions.

Filter	Mean X [px]	Mean Y [px]	Mean X [mas]	Mean Y [mas]
F380M	-0.0349 ± 0.042	-0.0381 ± 0.041	-2.2867 ± 2.742	-2.5018 ± 2.665
F430M	-0.0724 ± 0.030	0.0706 ± 0.032	-4.7518 ± 2.001	4.6283 ± 2.119
F480M	0.0681± 0.034	0.0681± 0.034	1.6659 ± 2.095	4.4698 ± 2.256

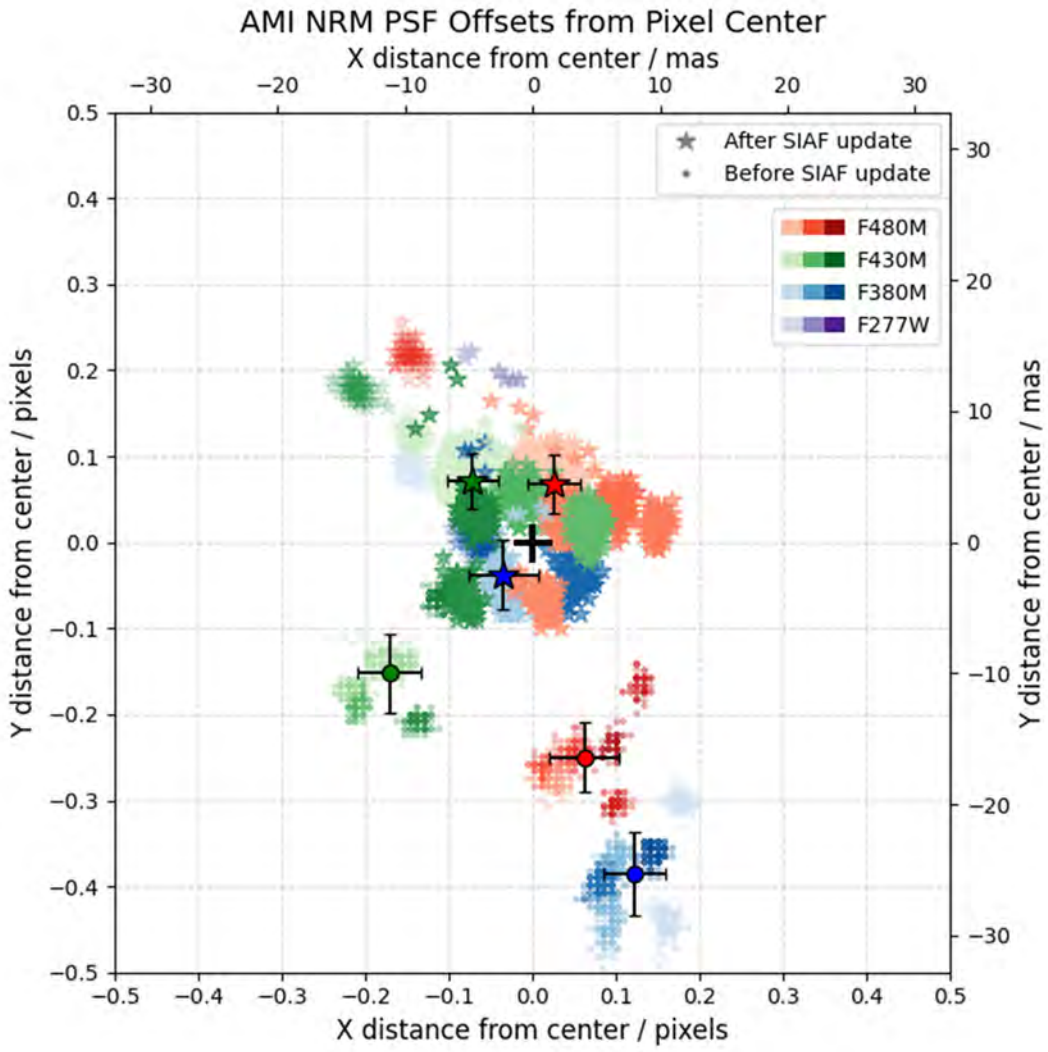

Figure 4. Measured offsets from the pixel center from before the SIAF update (commissioning), and from all primary-dithered reference star exposures after the per-filter apertures became active. As in Figure 1, the individual points or stars indicate offsets for each integration measured with the AK code, with the small clouds of points in the same shade being all the integrations in each exposure. The mean for each filter is indicated by the larger point or star with errorbars. The commissioning measurements differ from those in Figure 1 because the updated version of the AK code was used. Two exposures in F277W are included in the plot (purple stars), but we do not report a mean offset due to the scarcity of the data.

Figure 4 summarizes the improvements in AMI target placement before and after the updates. The mean offsets given in Tables 4 and 5 are represented by the larger points with error bars: round markers for commissioning data measurements and star markers for those that used the per-filter SIAF definitions, respectively. The area of the plot corresponds to one detector pixel and the black cross to the center of that pixel.

5.2 Anomalous exposures

After the initial analysis of all PSF reference star observations, three exposures were found to exhibit anomalously large offsets from their commanded positions and were therefore omitted from the mean offset calculation: jw002297002001_03107_0001, jw04611004001_03102_0001, and jw04611004001_03106_0001. After closer inspection, we found that 10 of the 25 pixels in the 5x5 cutout of the PID 2297 exposure had saturated and were replaced with NaNs by the pipeline, including the peak pixel, so there was not enough information in the PSF core to measure its location accurately. The two exposures from PID 4611 revealed unusually high drift over the duration of each exposure, resulting in a large standard deviation in offset across the integrations, though there were no indications of unsuccessful TA or guide star failure in the file header keywords. The measured offsets for each integration are plotted in Figure 5, beginning at the purple end of the colormap and ending at yellow. 4611:4:2 (left) had a duration of 57.7 s, and exposure 4611:4:6 (right) had a duration of 89.9 s.

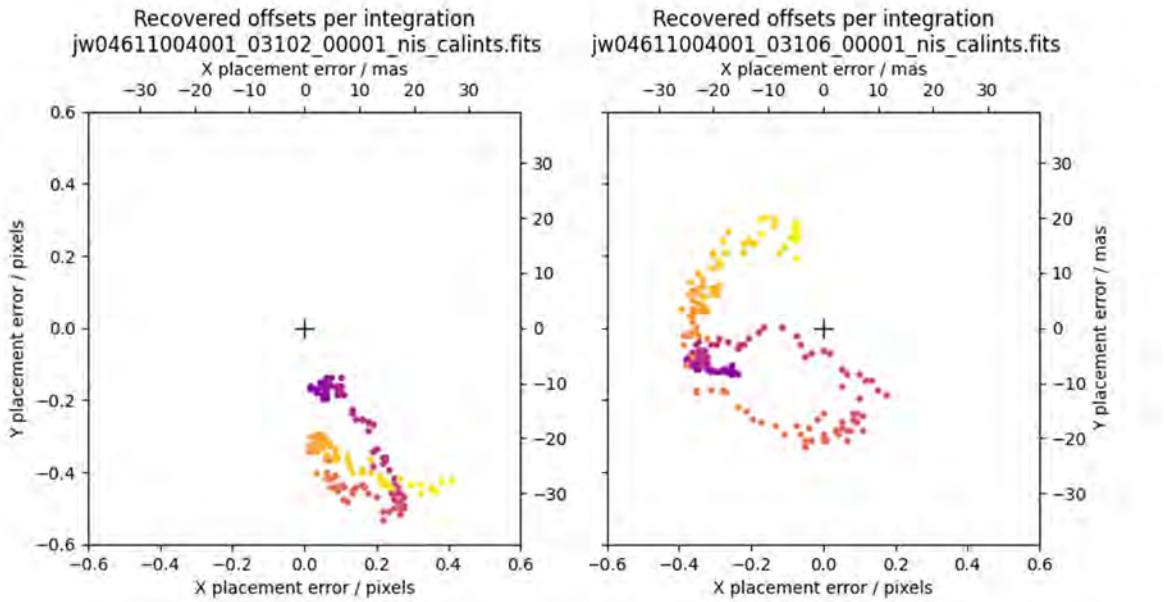

Figure 5. The measured position of two AMI reference star exposures during which fine guiding was paused due to higher-than-predicted guide star count rates. Each point indicates the offset from the commanded position in a single integration; the beginning of the exposure is the purple end of the colormap which progresses to the yellow points. These offsets were excluded from the mean offsets given in Table 5.

The guiding data retrieved by the TEL team revealed that the peak count rate had exceeded the predicted guide star bright limit for 89% of the duration of the exposure, during which fine guiding was suspended, allowing the target to drift. Photo response non-uniformity (PRNU) is a possible cause of the high count rate despite the mitigation efforts in place: the guide star amplitude tolerance was recently increased to 40%, from the launch threshold of 30% and the commissioning threshold of 35% (Warner et al. 2025). Nevertheless, the exposures were not automatically flagged as "bad," so the analysis presented in this report allowed us to identify that they were anomalies and inform the PI so they could request reobservation if the data

quality would affect their science goals for the program.

6 Conclusions

The SIAF update to use separate apertures for each filter that are offset relative to the primary dither position was found to be an effective way of reducing the positional error in AMI observations. Commissioning measurements found average offsets from the pixel center exceeding a quarter of a pixel for some filters. By using the opposite of these measured offsets to define new SIAF apertures for each filter, we were able to reduce the positional error to less than one tenth of a pixel for all three filters tested. The intrinsic pointing uncertainty remains, but the increased confidence in subpixel placement will allow proposers to leverage our understanding of pixel behavior to reduce contrast between PSF core pixels, thereby reducing charge migration, and split charge between adjacent pixels, allowing deeper observation of brighter objects.

The placement of AMI targets could likely be further improved by refining the aperture definitions based on the measurements presented in this report, but we have not yet confirmed that the potential benefits would warrant the up-front effort needed to make this incremental change. As analysis methods continue to improve and our understanding of charge migration behavior grows, we expect to reevaluate the requirements for exact AMI pixel placement.

7 References

Anderson, J. and King, I. R., 2000, “Toward High-Precision Astrometry with WFPC2. I. Deriving an Accurate Point-Spread Function”, PASP, 112, 1360

Goudfrooij, P., 2022, “Accuracy and Precision of Centroid Algorithms in the photutils Python package for NIRISS Point Spread Functions”, JWST Technical Report JWST-STScI-008116

Holfeltz, S. et al., 2015, “NIRISS Target Acquisition Centroid Simulations”, JWST Technical Report JWST-STScI-0003963

Perrin, M. et al., 2012, “Simulating point spread functions for the James Webb Space Telescope with WebbPSF”, Proc. SPIE 8842, 88423D

Perrin, M. et al., 2014, “Updated point spread function simulations for JWST and WebbPSF”, Proc. SPIE 9143, 91433X

Rigby, J. et al., 2022, “The Science Performance of JWST as Characterized in Commissioning”, PASP 135, 1046

Sivaramakrishnan, A. et al., 2023, “The Near Infrared Imager and Slitless Spectrograph for the James Webb Space Telescope. IV. Aperture Masking Interferometry”, PASP 135, 1043

Sivaramakrishnan, A. et al., 2023, “NIRISS Commissioning Results: NIS-019 NRM Performance (NGAS CAR-703, APT 1093)”, JWST Technical Report JWST-STScI-008334

Warner, G. et al., 2025, "JWST Fine Guidance Sensor Optimizations and Improvements since Launch", SpaceOps-2025, ID #228

A Appendix

Table A-1. Summary of additional AMI reference star exposures used to calculate the mean offset for each filter following the aperture updates.

Filename Base	Target	Filter	Ints	Groups	Exposure Start
jw01242010001_03102_00001_nis	HD 18638	F480M	4869	8	2023-10-31 11:18:09.962
jw01242010001_03104_00001_nis	HD 18638	F430M	6256	5	2023-10-31 12:16:54.595
jw01260104001_03102_00001_nis	HD17130	F480M	103	6	2024-09-16 23:42:47.185
jw01260104001_03104_00001_nis	HD 17130	F430M	137	4	2024-09-16 23:51:43.404
jw01260104001_03106_00001_nis	HD 17130	F380M	138	3	2024-09-17 00:00:34.013
jw04481001001_03102_00001_nis	HD 41094	F480M	760	30	2024-05-05 15:49:26.479
jw04481001001_03104_00001_nis	HD 41094	F380M	1060	11	2024-05-05 18:22:02.672
jw04481001001_03106_00001_nis	HD 41094	F430M	905	20	2024-05-05 19:46:51.279
jw04498026001_03102_00001_nis	GSPC P330-E	F480M	4	100	2024-06-10 17:49:44.970
jw04498026001_03104_00001_nis	GSPC P330-E	F380M	4	100	2024-06-10 17:52:19.594
jw04498026001_03106_00001_nis	GSPC P330-E	F430M	4	100	2024-06-10 17:54:43.018
jw04498026001_03108_00001_nis	GSPC P330-E	F277W	4	100	2024-06-10 17:57:12.522
jw04611002001_03102_00001_nis	HD 119164	F480M	145	4	2025-04-27 04:12:48.100
jw04611002001_03106_00001_nis	HD 119164	F430M	190	5	2025-04-27 04:19:52.791
jw04611006001_03102_00001_nis	HD 119164	F480M	145	4	2024-07-15 05:13:51.659
jw04611006001_03104_00001_nis	HD 119164	F380M	338	4	2024-07-15 05:16:41.419
jw04611006001_03106_00001_nis	HD 119164	F430M	190	5	2024-07-15 05:20:43.615
jw06606025001_03102_00001_nis	GSPC P330-E	F480M	4	100	2025-03-03 18:54:45.761
jw06606025001_03104_00001_nis	GSPC P330-E	F380M	4	100	2025-03-03 18:57:19.361
jw06606025001_03106_00001_nis	GSPC P330-E	F430M	4	100	2025-03-03 18:59:53.985
jw06606025001_03108_00001_nis	GSPC P330-E	F277W	4	100	2025-03-03 19:02:28.672

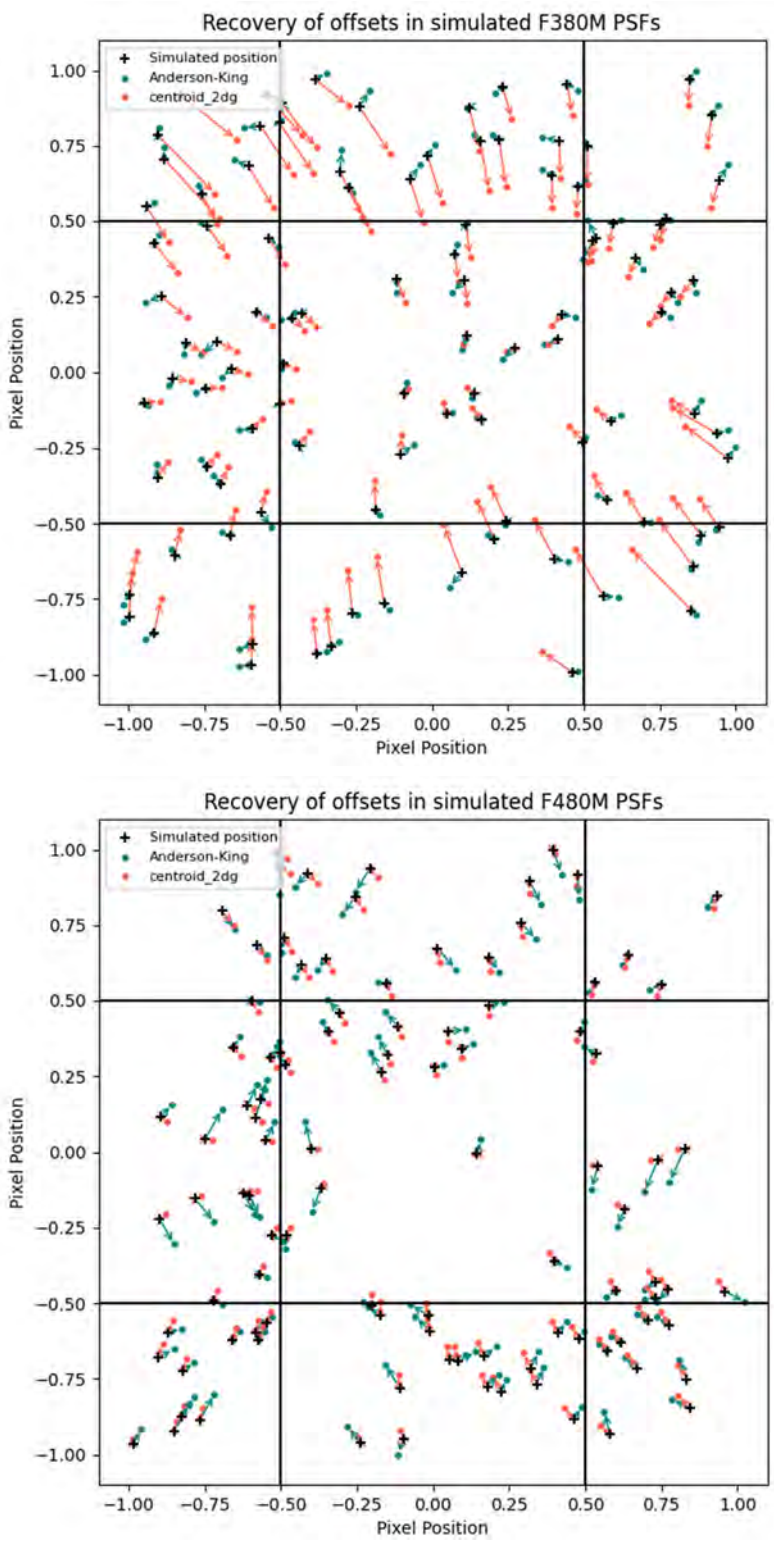

Figure A-1. Simulated positions of the test set of 100 simulated PSFs compared to the positions recovered by the Anderson-King and centroid_2dg codes, for F380M and F480M. The solid lines denote pixel boundaries.